

Keck Observations of the Hidden Quasar IRAS P09104+4109

Hien D. Tran¹, Marshall H. Cohen², and Montse Villar-Martin^{3,4}

ABSTRACT

We present imaging and spectro- polarimetric observations of the ultraluminous infrared galaxy IRAS P09104+4109 using the Keck 10-m Telescope. We detect the clear presence of broad $H\beta$, $H\gamma$, and Mg II $\lambda 2800$ emission lines in the polarized flux spectra of the nucleus and of an extranuclear emission region $\sim 4''$ away, confirming the presence of a hidden central quasar. The polarization of the broad Mg II emission line is high ($\sim 29\%$), consistent with the remarkably high polarization ($\sim 30\%$ – 40%) observed in the extended continuum emission. This indicates that the off-nuclear continuum is dominated by light scattered from the hidden quasar, most probably by dust mixed with the line emitting gas. The high polarizations, combined with the “foreshortened” morphology of the polarized brightness distribution allow us to constrain the scattering biconical structure to be at inclination $i \approx 50^\circ$ with a half-opening cone angle $\theta_c \approx 40^\circ$.

The narrow emission lines are polarized in a stratified fashion, with the high ionization lines ([O III], [Ne V], [Fe VII]) being polarized 0.7%–1.7% and [O II] essentially unpolarized. The line polarizations are positively correlated with critical density, ionization potential, and velocity width of the emission lines. This indicates that, as is the case with the narrow-line radio galaxies, which also often contain powerful quasars, the narrow-emission line region may be partially shadowed by the putative torus, with the higher ionization lines originating closer to the nucleus.

One notable characteristic of the extranuclear knot is that all species of Fe are markedly absent in its spectrum, while they appear prominently in the nucleus. In addition, narrow Mg II is observed to be much weaker than predicted by ionization models. Our favored interpretation is that there is a large amount of dust in the extranuclear regions, allowing gaseous refractory metals to deposit. Near the nucleus, dust is destroyed in the strong radiation field of the quasar, inhibiting metal depletion onto grains. The extended emission regions are most likely material shredded from nearby cluster members and not gas condensed from the cooling flow or expelled from the obscured quasar.

¹Department of Physics & Astronomy, Johns Hopkins University, Baltimore, MD 21218; tran@pha.jhu.edu.

²Astronomy Department, California Institute of Technology, Pasadena, CA 91125; mhc@astro.caltech.edu.

³Institut d’Astrophysique de Paris, F75014 Paris, France.

⁴Current address: Department of Physical Sciences, University of Hertfordshire, Hatfield AL109AB, UK; mvm@star.herts.ac.uk.

The higher temperature inferred from [O III] lines compared to that from [N II] and the general better agreement with models of line ratios, especially [O III] $\lambda 5007/\lambda 4363$ and He II/H β , provide strong evidence for matter-bounded clouds in addition to ionization-bounded clouds in the NLR. Ionization by pure velocity shocks can be ruled out. Shocks with photoionizing precursors may be present, but are probably not a dominant contributor to the energy input.

Subject headings: galaxies: active — galaxies: individual (IRAS P09104+4109) — galaxies: Seyferts — infrared: galaxies — polarization

1. Introduction

Discovered by the *IRAS* all-sky survey, ultraluminous infrared galaxies (ULIRGs, see review by Sanders & Mirabel 1996) emit most of their energy in the infrared ($L_{IR} > 10^{12} L_{\odot}$), and could harbor infant quasars enshrouded in a large amount of dust (Sanders et al. 1988). On the other hand, they may also represent energetic, compact starbursts (Condon et al. 1991; Genzel et al. 1998). Much recent research effort has been devoted to understanding the dominant energy source in these ULIRGs – whether it is obscured quasars or intense bursts of star formation.

IRAS P09104+4109 ($z = 0.44$; Kleinmann et al. 1988) is one of the few exceptionally luminous ULIRGs sometimes referred to as the “hyperluminous” ($L_{IR} \gtrsim 10^{13} L_{\odot}$) infrared galaxies. The others include F15307+3252 ($z = 0.926$; Cutri et al. 1994) and F10214+4724 ($z = 2.286$; Rowan-Robinson et al. 1991). All of these galaxies have been shown to harbor a quasar nucleus obscured from direct view (P09104+4109, Hines et al. 1999; F15307+3252, Hines et al. 1995; F10214+4724, Goodrich et al. 1996). This has led to the suggestion that perhaps all warm⁵ ULIRGs contain buried QSOs and that they may be the misdirected type 2 QSOs (AGN with Seyfert 2-like emission-line characteristics but QSO-like luminosities). A diagnostic diagram (Tran et al. 1999) involving [O III] emission line and infrared color f_{25}/f_{60} does indeed show that essentially all warm ULIRGs with sufficiently high ionization harbor energetic quasars in their centers.

IRAS P09104+4109 has been identified with a central cD galaxy in a rich cluster (Kleinmann et al. 1988; Hall et al. 1997). It has a high-ionization spectrum characteristic of a Seyfert 2 galaxy. Ground-based and *Hubble Space Telescope* (*HST*) images show that IRAS P09104+4109 has an off-nuclear northern extension or “plume” of ionized gas (Kleinmann et al. 1988; Hutchings & Neff 1988; Armus et al. 1999) that may serve as a scattering mirror of the light originating from the

⁵“Warm” ULIRGs are those having $f_{25}/f_{60} > 0.2$, Low et al. 1988; Sanders et al. 1988); f_{25} and f_{60} are the *IRAS* flux densities in units of Jy at 25 μm and 60 μm , respectively.

nucleus. We wish to probe the origin of this extension and constrain the scattering geometry for IRAS P09104+4109 by obtaining polarimetric observations of this knot.

In this paper, we confirm the high polarization and the broad emission lines of $H\beta$, $H\gamma$ and $Mg\ II$ in polarized flux of the nucleus. In addition to the B -band imaging polarimetry, we also present new spectropolarimetric data for the nucleus and off-nuclear emission regions of IRAS P09104+4109. We study in detail the emission-line spectra of the nuclear and extra-nuclear regions in order to derive an understanding of the ionization mechanism of the narrow-line region (NLR) of this galaxy. Throughout this paper, we assume $H_o = 75\ \text{km s}^{-1}\ \text{Mpc}^{-1}$, $q_o = 0$ and $\Lambda = 0$. At the redshift $z = 0.44$ of P09104+4109, $1''$ corresponds to a projected size of 5 kpc.

2. Observations and Reductions

Spectropolarimetric observations were made with the polarimeter (Cohen et al. 1997) installed in the low resolution imaging spectrometer (LRIS, Oke et al. 1995) on the 10-m Keck I telescope on the night of 1994 December 31 (UT). A $1''$ wide, long slit, was centered on the nucleus of IRAS P09104+4109, and oriented at $PA = 14^\circ$ to include the extended [O III] structure. The emission-line regions extend $\sim 5''$ north-northeast of the nucleus (Armus et al. 1999), as well as a few arcsecs south. We used a $300\ \text{grooves mm}^{-1}$ grating which provided a dispersion of $2.46\ \text{\AA pixel}^{-1}$ and a resolution of $\sim 10\ \text{\AA}$ (FWHM). The observations were made by following standard procedures of rotating the half waveplate to four position angles (0° , 22.5° , 45° , and 67.5°), and dividing the exposure times equally among them. Two sets of observations, lasting 60 and 52 min., were made under photometric conditions, giving a total exposure time of 112 min. The results presented here are the average of the two sets.

Spectra of the nucleus were extracted from an aperture $3''.4$ wide, and those of the NE off-nuclear region were extracted from a region $3''.6$ wide centered $3''.4$ from the nucleus. This includes the entire NE plume seen in the HST images by Armus et al. (1999). The data were reduced using VISTA, following standard polarimetric reduction techniques as described by Cohen et al. (1997). Hereafter, we shall refer to the nucleus spectrum as NUC and that of the NE extension as EXT.

Imaging polarimetry was obtained on the night of 1995 December 16 with the Keck I telescope. The images were taken through the B filter, which contains mainly continuum emission. Exposure times were 10 min. at each of the four waveplate positions. Sky was clear but seeing was variable between $1''$ – $1''.8$. Reductions were done analogously to spectroscopic observations as described by Cohen et al. (1997).

3. Results

3.1. Emission Line Ratios

Table 1 presents the integrated emission-line flux ratios with respect to $H\beta$ and their rest-wavelength equivalent widths for the NUC and EXT spectra, shown in Figure 1. The emission line fluxes of NUC were measured from the starlight-subtracted spectrum. The contribution from an old stellar population represented by the elliptical galaxy NGC 821 was used to remove the starlight. The starlight fraction ranges from 5% in the blue end to a maximum of 40% in the red. We did not correct for starlight in the EXT spectrum as the galaxy contribution in the outer regions is negligible. The largest source of uncertainty in the flux measurement is the placement of the continuum. For strong lines ($F/F(H\beta) \gtrsim 20\%$) the uncertainty is $\lesssim 10\%$; for weaker lines ($F/F(H\beta) \lesssim 20\%$) the uncertainty is 10%–25%.

The line ratios in NUC have been corrected for a small amount of extinction $E(B - V) = 0.24$ determined from the $H\gamma/H\beta$, and $H\delta/H\beta$ ratios, assuming the intrinsic case B values of 0.47 and 0.26, respectively (Osterbrock 1989), and the extinction curve of Cardelli, Clayton, & Mathis (1989) with $R_V = 3.1$. This correction is small and does not significantly alter the conclusions of this paper. No corrections have been applied to EXT as its observed Balmer line ratios are close to case B values, indicating little extinction due to foreground dust.

The small extinction derived might seem surprising, given the high infrared luminosity of this object. However, this is consistent with the result reported by Veilleux, Kim & Sanders (1999) in their spectroscopic study of a large sample of ULIRGs, that there is no obvious correlation between extinction and IR luminosity among the IR-bright galaxies. The mean $E(B - V)$ for the Seyfert 2 galaxies in their sample is 1.2 with a range of 0.3 to 2.7. Our reddening estimate is intermediate between those found by Kleinmann et al. (1988, $E(B - V) < 0.12$), who used the same optical line ratios, and Soifer et al. (1996, $E(B - V) = 0.38$ – 0.79), who used infrared [S II] and hydrogen lines in combination with optical lines. Soifer et al. also suggested that the low reddening may result from the dust being confined in a disk-like structure, which effectively obscures the central nucleus but does not block our line of sight to the NLR. As Veilleux et al. (1999) noted, the color excess derived from the optical line ratio method tends to underestimate the amount of dust in these objects.

In the nucleus, the narrow lines all display a strong blueward asymmetry, as reported by Kleinmann et al. (1988), Crawford & Vanderriest (1996) and Hines et al. (1999), and cannot be adequately fit with a single Gaussian profile. Two Gaussian profiles including a main, central component with (intrinsic) FWHM $\approx 600 \text{ km s}^{-1}$ and another component blueshifted 720–980 km s^{-1} with FWHM $\approx 700 \text{ km s}^{-1}$ are able to fit the observed profiles well. Our measured range of velocity shifts of the blue-shifted component is somewhat smaller than the 1250 km s^{-1} reported by Crawford & Vanderriest (1996), and more consistent with 950 km s^{-1} reported by Kleinmann et al. (1988).

Aside from the smaller line widths in EXT, the most remarkable difference between the NUC and EXT spectra is the complete absence of any Fe species in EXT, as Figure 1 shows.

3.2. Imaging Polarimetry

The imaging polarization of IRAS P09104+4109 is shown in Figure 2. The polarization is very high ($\sim 25\%$ – 30%) throughout the nucleus and extensions up to $5''$ away. The polarization increases strongly across the source. In the south, a number of pixels shows $P > 30\%$, and the highest is $40.3\% \pm 12.8\%$. We note that the distribution of surviving vectors is biased because those which have positive errors are preferentially saved; however, there is no doubt that the polarization is remarkably high.

Unlike most of the narrow-line radio galaxies like 3C 195 and 3C 33 (Cohen et al. 1999), there is no well-defined V-shape bi-cone of scattered light, although the entire region is highly polarized. The polarization field displays a strong similarity to the patterns in the BLRG FSC 2217+259 and the highly-polarized NLRG 3C 234 (Tran 1995; Cohen et al. 1999). To the NE and SW, the vectors are perpendicular to the radius and this suggests scattering from a central illuminating source. However, the curvature of the polarization vectors is small, as in 3C 234 and FSC 2217+259. This may suggest that the viewing angle is small, indicating that the line of sight is just outside the ionization cone (see §4.3), a geometry that has also been suspected in 3C 234 (Tran et al. 1995; Cohen et al. 1999).

The southern extension appears to display somewhat higher polarization than its northern counterpart. This may be a result of forward scattering and would imply that the cone axis is pointed toward us in the south, analogous to Cygnus A (Ogle et al. 1997). Dilution by line emission is not a major factor since there are no strong emission lines through the B band used. However, dilution by hot stars or nebular continuum could play an important role in the north as there is more ionized gas there. Our imaging polarimetry confirms and extends the polarization map obtained with *HST* by Hines et al. (1999), which shows a reflection “cone” in the central $1''$.

The right panel of Figure 2 shows the polarized flux $P \times F$ which is commonly called the “polarized light”. As can be seen, the polarized light distribution extends more to the north than to the south, reaching up to $\sim 4''$ (20 kpc) to the northeast along $PA = 19^\circ$. This coincides well with the extended [O III] emission seen in the ground-based (Kleinmann et al. 1988) and *HST* images (Armus et al. 1999). The polarized extension is thus better aligned along this emission-line structure ($PA \approx 11^\circ$) than the radio axis ($PA = 333^\circ$), a condition also exhibited by many high and low-redshift radio galaxies (Tran et al. 1998; Cohen et al. 1999). This indicates that EXT serves as a reflection region of nuclear light, and that it lies exposed to the ionizing radiation escaping through the ionization cones from the hidden quasar. The polarized flux distribution peaks at the total flux peak, suggesting that scattered light dominates the observed radiation.

3.3. Spectropolarimetry

3.3.1. Nucleus

The spectropolarimetry for NUC is displayed in Figures 3. High polarizations are seen, with magnitudes consistent with those seen in the imaging polarimetry (Fig. 2). The Keck data of the nucleus confirm the general results of Hines et al. (1993, 1999). The observed continuum polarization uncorrected for starlight ranges from $\sim 8\%$ at 6000 \AA (rest) to about 18% at 3000 \AA (rest). The polarization PA is constant with wavelength at 97° . In addition to broad $H\beta$, $H\gamma$, and probable Fe II multiplets near 3200 \AA reported by Hines et al., we also detect broad Mg II in polarized flux. We measured a FWHM of $7540 \pm 700 \text{ km s}^{-1}$ for the broad $H\beta$ in polarized flux, somewhat smaller than that reported by Hines et al. (1999, $12,000 \pm 2500 \text{ km s}^{-1}$). This is comparable to the FWHM of $6000 \pm 700 \text{ km s}^{-1}$ measured for $H\gamma$. The resemblance of the nuclear $P \times F_\lambda$ to a quasar spectrum also extends to its shape.

The galaxy-corrected total flux spectrum F_λ ($\alpha = -0.94$, $f_\nu \propto \nu^\alpha$) is redder than $P \times F_\lambda$ ($\alpha = -0.46$), which is similar in slope to the more core-dominated composite QSO spectrum of Baker & Hunstead (1995, $\alpha = -0.5$), or that of Francis et al. (1991, $\alpha = -0.32$). Our measured spectral indices agree well with those of Hines et al. (1999). This suggests that there is a second “featureless continuum” FC2 in the total flux spectrum that makes it redder. This component is likely due to a combination of hot stars and nebular continuum plus reddened transmitted light from the hidden AGN (e.g., Cohen et al. 1999). Quasars viewed at high inclination angle have been shown to exhibit redder continuum due to dust extinction (Baker 1997). The presence of hot stars, perhaps arising in a starburst, is suggested by the broad feature underlying He II $\lambda 4686$. This feature cannot be a broad scattered He II component since it appears very strongly in the total flux spectrum, suggesting that the light is viewed directly, and it is not detected in the $P \times F_\lambda$ spectrum (see Fig. 3). It can be attributed to Wolf-Rayet (W-R) stars, as has been identified by Heckman et al. (1997) in Mrk 477 and Storchi-Bergmann, Cid Fernandes, & Schmitt (1998) in Mrk 1210, and Tran et al. (1999) in TF J1736+1122.

In addition, there is nebular continuum giving rise to the Balmer jump near 3650 \AA . If this is the case we would expect the Balmer jump to be unpolarized. Is it? To answer this, we have constructed an “unpolarized spectrum” $= F_\lambda - (1/0.20) \cdot P \times F_\lambda$, assuming an intrinsic continuum polarization of 20% . We then measured the Balmer jump index defined as f_{3727-}/f_{3727+} , where f_{3727-} is the continuum flux just blueward of [O II] $\lambda 3727$, and f_{3727+} that just redward of it. We obtain an index of 1.74 ± 0.1 for the total flux spectrum, and 2.0 ± 1 for the unpolarized flux. Naturally, there is a larger uncertainty in the value obtained from the unpolarized flux spectrum. However, a Balmer discontinuity appears to still be present, meaning that it is unpolarized, and supporting the notion that FC2 contains nebular continuum plus starlight from a starburst.

We find that P_s , the intrinsic polarization⁶ produced by scattering, is $P_s(H\beta) \approx 16\%$ while $P_s(\text{Mg II}) \approx 29\%$ (see below). This strengthens the reality of the nebular continuum discussed

⁶We refer to the continuum-subtracted polarization of the broad emission line as the “intrinsic polarization”.

above, since a rising P_s toward the blue would leave most of the Balmer discontinuity in the unpolarized flux spectrum. This blue P_s is possible with dust but not electron scattering. Thus, dust scattering is important, while electron scattering could contribute but not dominantly.

3.3.2. *Extension Polarization Spectrum*

The polarization of EXT is noisier than NUC, and we have binned the results (except for F_λ), presented in Figure 4, by 5 pixels to improve S/N. As can be seen, the polarization shows similar behavior and magnitude to those in NUC. In addition, a broad Mg II is clearly seen in the total flux spectrum. This indicates that the continuum in EXT is dominated by scattered light from the obscured quasar. The polarization PA is roughly constant with wavelength at $106^\circ \pm 2^\circ$, slightly higher than that measured in the nucleus. The PA is accurately perpendicular to the slit, as expected for an off-nuclear measurement of a reflection nebula (see Cohen et al. 1999 for similar cases).

We show the EXT $P \times F_\lambda$ smoothed by 7 pixels in Figure 5, which shows clearly that broad H β and Mg II are present. In $P \times F_\lambda$, the spectral index is $\alpha = +0.5$, significantly bluer than the average quasar spectrum. Assuming that the incident spectrum is typical for a quasar, this suggests that, as for the nucleus component, dust is the dominant scatterers which could bluen the light.

3.3.3. *Modeling of the Broad Line Polarization*

We model the spectropolarimetric observations using the procedure described by Tran et al. (1997), to separate the various components of the emission lines and continuum. In a region surrounding the [O III]+H β complex, we perform a fit of the continuum and emission-line components in the total flux, $Q \times F_\lambda$, and $U \times F_\lambda$ spectra. The broad H β is assumed to have the same profile as in the polarized flux spectrum. The narrow lines of H β and [O III] were fitted assuming that they are similarly polarized, and consist of one main core component and another blue-shifted component, both with Gaussian profiles. Our Keck data do not have sufficient spectral resolution to warrant the addition of more than two components in the [O III] profile, and we do not attempt to fit the line polarizations with the three narrow components identified by Hines et al. (1999). The results indicate that the continuum and broad H β are similarly polarized at $16\% \pm 3\%$ and $PA = 98^\circ$.

Similar modeling at the Mg II line shows that the polarization of the broad Mg II line, at 29%, is substantially higher than broad H β , but is consistent with values seen in the imaging polarimetry. If real, it suggests that the intrinsic polarization rises to the blue, which is only possible if dust scattering is present.

Our fitting also shows that the core component of the narrow [O III] lines has a small amount of polarization, $0.70\% \pm 0.03\%$ at $PA = 90^\circ$, which is different from that of the broad line and continuum. On the other hand, the [O II] $\lambda 3727$ line is virtually unpolarized. We measure a polarization of $0.22\% \pm 0.12\%$. This indicates radial stratification of the NLR gas (see below).

3.3.4. Stratification of Narrow-Line Polarization

The high S/N data allowed us to measure the polarization of various emission lines in the nucleus. The results are in Table 2, where we list the (biased) P , θ , their associated errors, the ionization potential (IP) of the lower and upper stages of ionization for the ions of interest, and the critical density (n_{crit}) for collisional de-excitation of each line (calculated at 10^4 K). The polarizations are flux-weighted means in the core component only, and the uncertainties on P and θ are 1σ statistical errors alone and do not include systematics such as those due to continuum placement and data reduction. In Figure 6, we plot the measured line polarizations versus n_{crit} , the mean of the lower and upper IP, and FWHM. A clear trend is apparent in all three plots: lines of higher n_{crit} , IP and FWHM exhibit higher polarization. Such a correlation has also been observed in the LINER NGC 4258 (Barth et al. 1999). To our knowledge, NGC 4258 and IRAS P09104+4109 are the only two AGNs where this phenomenon has been shown to occur systematically over a number of forbidden lines with a wide range of ionizations. The tendency for [O III] to be more polarized than [O II], especially in radio galaxies (di Serego Alighieri et al. 1997), has been known for some time, and an anisotropic [O III] emission structure has been suspected as the cause (Hes, Barthel, & Fosbury 1993). Together with the well-known correlation of linewidth with n_{crit} and IP (e.g., De Robertis & Osterbrock 1986) in Seyfert galaxies, this result provides strong indication that the narrow emission-line structure in IRAS P09104+4109 is radially stratified, with lines of higher ionization and critical density being emitted closer to the nucleus, and therefore more likely to be partially occulted. The higher polarization results from less dilution by direct light.

3.4. Physical Conditions and Diagnostic Diagrams

The temperature determined from the [O III] $\lambda 5007$ /[O III] $\lambda 4363$ ratio (using Table 1) is $\approx 1.3 \times 10^4$ K for both NUC and EXT. We also used the [N II] $\lambda 6583$ line from the near-IR spectrum of Evans et al. (1998) to measure the temperature from the [N II] $\lambda 5755$ / $\lambda 6583$ ratio. This is only available for NUC, giving $T_e = 9000$ K. This is about 4000 K cooler than the [O III] region, and may suggest that matter-bounded clouds are present (e.g., Wilson et al. 1997). The electron density estimated from the [Ar IV] $\lambda 4712$ / $\lambda 4740$ ratio is $\approx 10^4 \text{ cm}^{-3}$ and $5,000 \text{ cm}^{-3}$ for NUC and EXT, respectively. This can be compared to a value of $6,000 \text{ cm}^{-3}$ for NUC determined from [Cl III] $\lambda 5518$ / $\lambda 5538$ line ratio. The [Ar IV] $\lambda 4712$ / $\lambda 4740$ ratio is clearly better determined than the [Cl III] $\lambda 5518$ / $\lambda 5538$ ratio since the stronger Ar lines are less affected by starlight subtraction and

yield more certain flux measurements.

To help us understand the rich emission-line spectrum of IRAS P09104+4109, we compare the line ratios with model calculations. In particular, we would like to understand the source of the ionization and the excitation mechanism of a large number of emission lines encompassing a wide range of ionization, from the low-excitation [N I] λ 5200, and [S II] to the coronal lines such as [Ne V] and [Fe VII]. Theoretical models from three main mechanisms are considered:

1) Simple photoionization of essentially radiation-bounded NLR clouds by the central source having a powerlaw radiation spectrum. The emergent emission-line spectrum is characterized by the slope α of the ionizing continuum, and the ionization parameter $U = Q/4\pi r^2 c n_e$, where Q is the number of ionizing photons, r is the radius and n_e is the electron density. We build the AGN models with the photoionization code MAPPING Ic (Ferruit et al. 1997), using a power-law with index $\alpha = -1.5$. The models are isobaric, so the density varies across the nebula. Recently, a new set of models has been computed for the NLR in an attempt to account for more realistic physical conditions. In these models the line emission originates from a wide range of temperatures and densities, although the observed emission-line spectrum results only from clouds best able to emit it. These are called “locally optimally emitting clouds” (LOC) models (Ferguson et al. 1997a, 1997b). We shall discuss these models but compare our observations only with the simple, isobaric calculations that we made.

2) Two-component photoionization model of Binette et al. (1996, 1997), consisting of both optically thin gas (matter-bounded, MB) clouds and optically thick gas (ionization-bounded, IB) clouds. The sequence is parameterized by the parameter $A_{M/I}$ which is the ratio of the solid angle subtended by MB clouds relative to that of IB clouds, as viewed by the observer. Most of the higher ionization lines (i.e., coronal lines and [O III]) are emitted by MB clouds, which lie closer to the nucleus, filtering the radiation field that reaches the IB clouds further away, where essentially all of the lower ionization lines (e.g, [N II], [O I]) originate (Binette et al. 1996; Binette et al. 1997). A large value of $A_{M/I}$ indicates a larger weight to the MB component, and therefore a higher excitation spectrum.

3) Shocks and shock + precursors models of Dopita & Sutherland (1995, 1996). Mechanical energy deposited by velocity shocks due to turbulent cloud motions or the outflowing radio jets can produce powerful local UV radiation which can ionize the gas. Two types of shock models have been considered: pure shocks, in which mechanical energy from shocks is solely responsible for collisionally heating the gas, and the hybrid shocks + precursors, also known as “photoionizing shocks”, in which the shock itself generates an abundant supply of ionizing photons in the hot post-shock gas and produce an extensive precursor H II region.

3.4.1. Comparison to Model Predictions

In Figures 7–8, we present several diagnostic diagrams involving a number of emission lines with a wide range of ionization as an attempt to identify the main underlying mechanism for ionizing the NLR gas in NUC and EXT. Model calculations based on the above three mechanisms are shown for comparison with the observations. Simple power-law U sequences are plotted for density $n_e = 10^4 \text{ cm}^{-3}$ (of the front layer) as determined from the nuclear gas. Sequences with $n_e = 5000 \text{ cm}^{-3}$ (as determined from the extended gas) produce very similar results and we do not plot them on the diagrams. Two different sequences are shown for the IB+MB photoionization models of Binette et al. (1997), each characterized by the value of the ionization parameter *at the irradiated face of the MB component*, U_o : high $U_o = 0.5$ and low $U_o = 0.05$. The ionization parameter of the IB component is 6.5×10^{-4} for both. On all figures, the parameter $A_{M/I}$ goes from 0.01 to 100, increasing from left to right. Pure shocks and shocks + precursors models are plotted as grids parameterized by the shock velocity V and the magnetic parameter B/\sqrt{n} . V varies from 150 to 500 km s^{-1} , and B/\sqrt{n} varies from 1 to 4 $\mu\text{G cm}^{-3/2}$. All models are shown for solar abundances.

The symbols have the following meanings: star denotes EXT and open circle represents the total line flux from both the core and blue-shifted components in NUC. The solid and open triangles indicate the core and blue-shifted emission line components of NUC, respectively. We shall now discuss these diagrams.

3.4.2. Shocks and AGN photoionization

Figure 7 shows that in two of the best optical diagrams for shock diagnostics, ([O III] $\lambda 5007/\lambda 4363$ vs. He II $\lambda 4686/\text{H}\beta$ proposed by Clark et al. 1997, Villar-Martin et al. 1999, and [Ne V] $\lambda 3426/[\text{Ne III}] \lambda 3869$ vs. [O III] $\lambda 5007/\text{H}\beta$ proposed by Allen et al. 1998), the positions of the NUC component lie well outside the range of model grids predicted by pure shocks and shocks + precursors. The shock + precursor models are a little more consistent with the points for the EXT gas. These diagrams clearly reject pure shock as the dominant emission line mechanism in both the nuclear and extra-nuclear regions of IRAS P09104+4109, as it tends to predict too low [O III] $\lambda 5007$. On the other hand, ionization-bounded AGN photoionization models have the opposite problem, failing to agree with the observed data by predicting too high [O III] $\lambda 5007$.

The presence of dust (see §3.3, 4.1) in the EXT also weakens considerably any arguments that shocks play a dominant role in the main energy input mechanism. If shocks were present the dust grains would likely be destroyed (Donahue & Voit 1993; de Young 1999). Another argument against shocks is that the radio and emission line “cone” in IRAS P09104+4109 are *misaligned* by as much as 38° (Hines et al. 1999), making shocks induced by the nuclear jets unlikely. Also, the [O III] $\lambda 5007/[\text{O II}] \lambda 3727$ line ratio (a good indicator of the ionization parameter U) is

observed to be 5.4 for NUC and 2.11 for EXT. Thus U does not go up or remain constant in the extra-nuclear regions, as would be the case if shocks + precursors provide extra local heating (e.g., as in 3C 299, Feinstein et al. 1999), but actually drops, as expected from geometric dilution of the radiation field. Finally, the velocity widths of the emission lines in the extension are essentially unresolved $< 550 \text{ km s}^{-1}$, indicating that perturbations in the gas velocity by shocks, if any, are small.

In conclusion, we can rule out pure shocks as the ionizing mechanism. Shock + precursors are also ruled out in the nuclear region, but it is more ambiguous whether they exist in the extension. Crawford & Vanderriest (1996) have suggested that shock heating may increasingly become important in the extended gas. However, we do not find sufficient evidence in our data to support a dominant role by shocks even in the extensions. More conclusive resolution between shocks and photoionization may come from additional diagnostics using UV lines (Dopita et al. 1997; Allen et al. 1998), which are more sensitive to shocks than optical lines.

3.4.3. *The Need for Matter-Bounded Clouds*

As Figure 7 indicates, the models for the high-density IB photoionization sequence predict too high [O III] $\lambda 5007$, typically giving $[\text{O III}]/\text{H}\beta \gtrsim 16$. This has been a well-known problem for IB photoionization models, known as the “temperature problem”: the models predict too low a [O III] $\lambda 4363/\lambda 5007$ ratio and thus too low electronic temperatures (i.e., Binette et al. 1996). One attractive possibility that may solve this discrepancy is with the addition of MB clouds. As already mentioned, the presence of MB clouds is suggested by the higher temperature in the [O III] emitting region compared to that in the [N II] emitting region in the nucleus, since the MB clouds, where most of the [O III] originates, are expected to lie closer to the ionizing source (Binette et al. 1996; Wilson et al. 1997).

In Figure 8, we present additional diagnostic line ratios with comparison to the IB + MB as well as shock + precursor models. The top two panels are the same as Figure 7. As can be seen, the shock + precursor models clearly fail to fit all the NUC data points and miss the EXT points in most diagrams. In general, the addition of MB clouds is able to resolve the two main difficulties of pure IB photoionization models: lines ratios of He II/ $\text{H}\beta$ and [O III] $\lambda 5007/\lambda 4363$. However, these sequences also have problems. For example, a common problem for all photoionization models is that [Ne V] is overpredicted (Fig. 8, top right). Note also that only models with $A_{M/I} < 1$ are able to fit the observed He II, but they have difficulty reproducing the high [O III] $\lambda 5007/\text{H}\beta$, especially the low U_o sequence (solid curve). The high U_o sequence (dotted curve in the plots) is consistent with *both* the observed He II and [O III] ratios, but it cannot reproduce the low-ionization lines [O II]/ $\text{H}\beta$, [N I]/ $\text{H}\beta$ and [S II]/ $\text{H}\beta$, which are predicted to be too strong. The low U_o sequence has the opposite problem, agreeing well with these low-ionization lines but failing to explain higher ionization lines like [Ne V] and [Fe VII], as well as the weakness of He II for the observed [O III]/ $\text{H}\beta$. Since it is the contribution from MB clouds that makes it possible to solve the He II and

temperature problems, and since the low-ionization lines are mostly due to the IB component, a higher ionization parameter for the IB component might be consistent with all data (recall that Binette et al. 1996 used a fixed $U[\text{IB}]$).

In summary, Figure 8 shows that shocks + precursors models fails to reproduce the observed data points in NUC and, to a lesser degree, in EXT. Photoionization models with contribution from matter-bounded clouds are able to reproduced the data well, although no single photoionization sequence is perfect.

4. Discussion

4.1. Dust in the Extended Emission-Line Gas

In §3.3, we presented polarimetric evidence for dust in the scattering regions. Diagnostic line ratios also show evidence for dust in the emission line gas.

4.1.1. High-Ionization and Fe lines

One of the most notable features of the emission line spectra of IRAS P09104+4109 is the conspicuous absence of all species of Fe in EXT and their strong presence in NUC (see Fig. 1 and Table 1). No other atomic species other than iron is seen to exhibit this behavior. This dramatic difference in Fe line strength between NUC and EXT cannot be due to the lack of high ionization photons in EXT, for we see clearly in EXT strong high-ionization lines of [Ne V], which has comparable ionization potential (97.1 eV) to [Fe VII] (100.0 eV). Furthermore, lower ionization Fe lines like [Fe VI], [Fe V] and perhaps [Fe III] are all completely absent from EXT. Coronal lines can be expected to be seen in the tenuous off-nuclear extended gas (Ferguson et al. 1997b), and indeed [Ne V] is seen in our EXT spectrum, and [Fe IX] has been observed in the extended emission line regions of Circinus (Oliva et al. 1994; Moorwood et al. 1996), Cygnus A (Ogle et al. 1997) and Tololo 0109–383 (Murayama, Taniguchi, & Iwasawa 1998).

The peak range of the line strength distribution function in the LOC models of Ferguson et al. for [Ne V] and [Fe VII] overlap substantially with each other. Therefore, under “ordinary” NLR conditions (i.e., solar abundances, free of dust) we would expect to see [Fe VII] wherever [Ne V] is seen. If [Fe VII] is as strong relative to other lines as observed in the nucleus, there should be no problem detecting it in EXT. In NUC, [Fe VII] $\lambda 6087$ is about 3 times weaker than [Ne V] $\lambda 3246$ and 5.6 weaker than $\text{H}\beta$. At this level, [Fe VII] should be even stronger than [N I] $\lambda 5200$, or about as strong as He I $\lambda 4471$, both of which are clearly seen in EXT. Even if it is 6–13 times weaker, as predicted by models of Binette et al. (1997) or Ferguson et al. (1997), it should be at least about as strong as [Ar IV] $\lambda \lambda 4712, 4740$ or He I $\lambda 5876$. Somehow, virtually all gaseous Fe is removed from the extension gas. With the inclusion of dust grains, [Fe VII] is expected to be

about 74 times weaker than [Ne V] (Ferguson et al. 1997b). At this level, it would be impossible to detect with our data. This strongly suggests that there is significant amount of dust in the extension allowing gas-phase Fe to deplete onto grains. This notion has been invoked to explain the emission-line spectra of Seyfert galaxies (Kingdon, Ferland, & Feibelman 1995). Neon is an inert gas and not expected to be depleted (see model calculations by Ferguson et al. 1997b). [Fe VII] $\lambda 6087$ is a coronal line, and both Ferguson et al. (1997b) and Binette et al. (1997) have suggested that coronal lines are not efficiently emitted in gas with dust. The lack of [Fe VII] $\lambda 6087$ in EXT therefore is consistent with the presence of dust.

It is unlikely that the absence of Fe lines in EXT is due to the lower metallicity of the EXT region, for other metals such as oxygen and nitrogen seem to be well represented. We would expect Fe to show a normal abundance as there exists a well-known [Fe/H] to [O/H] relation for the nebula gas observed in the solar neighborhood and galactic bulge (e.g., Maciel 1999).

4.1.2. *Narrow Mg II*

Another element which may lend itself well to diagnostics for dust is Mg since it is about as sensitive as Fe to depletion. Unlike the higher-ionization forbidden Fe lines, Mg II is complicated by several factors. It is a resonance line so it can be strongly affected by intervening dust extinction and gas absorption. On the other hand, like other low-ionization lines such as [S II], [O II], [N II] it may even get strengthened by photoelectronic heating of the gas by dust grains (Ferguson et al. 1997a).

With these caveats, we now consider whether the resonant character of Mg II $\lambda 2800$ and its strong sensitivity to dust and gas absorption suggest the presence of dust as well. Figure 9 shows the diagram of Mg II $\lambda 2800$ /[O II] $\lambda 3727$ vs. [O III] $\lambda 5007$ /H β . The MB + IB photoionization models predict Mg II to be stronger than observed in both the nuclear and extended gas. Shock + precursor models show reasonable agreement to the data, but they fail for most other lines, and have been eliminated for the nuclear emission (see §3.4.2, 3.4.3). One way to weaken Mg II $\lambda 2800$ without dust is with intervening absorbing gas, containing Mg II. Since Mg II is in ionized form, the most likely explanation is that the absorbing gas is in the ionized cones. We compare the predictions of the photoionization models taking into account viewing effects: depending on the viewing angle of the observer relative to the clouds, the spectrum of the resonant lines, like Mg II $\lambda 2800$ will be different (Villar-Martin, Binette & Fosbury 1996). If the clouds are viewed from the illuminated face, the Mg II emission will be relatively stronger than when seen from behind. In the former case, the photons find a lower column density of Mg II (since the gas is highly ionized towards the illuminated face) and they can escape the nebula freely. However, photons that try to leave the cloud through the “non-illuminated” face of the cloud will encounter a much larger column density of Mg II and will be repeatedly absorbed.

In Figure 9 we show this effect. The upper thick solid line shows the line ratios for a nebula

viewed from the illuminated surface. The lower thick solid line shows the line ratios for a nebula seen from behind. As can be seen, the difference is large. These models show that we need to view the clouds directly from the back (the non-illuminated side) to reduce the Mg II emission to the low observed values. However, this extreme view is probably not the case, for if the clouds are seen from behind, the observer would be inside the ionization cone and therefore, would have a full view of a quasar or broad line radio galaxy. Another possibility is that the absorbing gas is outside the ionized cones, but in this case the ionization of the gas cannot be explained.

Thus again, the most reasonable explanation is that the emitting gas contains dust. It could be due to depletion (Mg is about as sensitive to depletion as Fe), or to a combination of resonant scattering and dust absorption. Pure resonant scattering alone cannot explain the weakness of the line. This conclusion is consistent with the indication for dust from the absence of Fe lines, as well as the polarized flux spectrum, which is blue compared to a composite quasar spectrum (§3.3.2).

4.2. Origin of the Extended Gas

While the indication for dust in the nucleus and extended emission regions of IRAS P09104+4109 comes as no surprise from one of the most luminous infrared emitters, this confirmation shows that the existence of dust is extensive over a large scale, and could have important implications for the origin of the extended gas.

As suggested by Donahue & Voit (1993) for the intracluster nebular gas that they studied, the presence of dust inferred in the extension implies that EXT cannot be gas condensed directly out of the X-ray emitting intra-cluster medium (ICM). This is because dust simply cannot survive in the hot ICM in any appreciable amount. Any dust introduced in the hot ICM is expected to be destroyed long before the gas is cooled enough to be visible or gets transported to the cluster center by the cooling flow. Villar-Martin & Binette (1997) reached a similar conclusion in their finding of dust in the extended emission-line regions of radio galaxies.

Since there is no evidence that the metal abundances are anomalously low (§4.1.1), the most likely candidate for the extended gas is perhaps shreds of unfortunate members of the cluster being cannibalized by IRAS P09104+4109. Active star forming regions, either in the galaxies themselves or triggered by the interactions, are where copious amounts of dust are found. This in turn implies that the extranuclear gas is unlikely to be material expelled or outflowing from the nucleus of the central quasar. *HST* WFPC2 imaging of IRAS P09104+4109 by Armus et al. (1999) does indeed show what seem like whiskers and filaments, suggestive of stripped remains from nearby cluster members. In addition, recent *HST* WFPC2 and NICMOS imaging studies of ULIRGs by Surace et al. (1998) and Scoville et al. (2000) have shown that many galaxies contain numerous circumnuclear clusters of bright young stars (age $\sim 10^7$ – 10^8 yrs), whose forming regions are often associated with dust.

The external origin for the gas is supported by the fact that many ULIRGs show evidence for

interaction or merging (e.g., Duc, Mirabel & Maza 1997; Borne et al. 2000; Scoville et al. 2000), which has been suggested to stimulate the ULIRG phase. Velocity structure of the extended nebula of IRAS P09104+4109 derived from integral field spectroscopy by Crawford & Vanderriest (1996) also suggests that the gas is probably external in origin. However, these authors do not favor the picture of the gas being merged with the cD galaxy, based on the low relative velocity ($\sim 100\text{--}200 \text{ km s}^{-1}$) with respect to the nucleus.

4.3. Scattering Geometry

The polarizations of ULIRGs with hidden broad-line regions are generally very high ($\sim 20\%\text{--}30\%$), suggesting that the inclination angle could be fairly substantial ($\gtrsim 35^\circ$). Under the assumption that the lack of a well-defined V-shape polarization fan suggests that the inclination angle i does not exceed the half-opening cone angle θ_c by a large amount, we can use the morphology of the polarization image (Fig. 2) to constrain the scattering geometry of IRAS P09104+4109, using the model of Brown & McLean (1977) (see also Miller & Goodrich 1990; Miller et al. 1991; Wills et al. 1992; Balsara & Krolik 1993; Brotherton et al. 1998). Analysis by Hines et al. (1999) has constrained the viewing inclination and half opening cone angle lie in the range $34^\circ < i < 41^\circ$ and $15^\circ < \theta_c < 33^\circ$, based on $P = 20\%$. With our higher polarization of $\sim 30\%$ from the broad Mg II and imaging polarimetry, these limits are still consistent, but we can eliminate the combination of both upper limits or lower limits for i and θ_c (i.e., $i = 41^\circ$ $\theta_c = 33^\circ$, or $i = 34^\circ$ $\theta_c = 15^\circ$), as they give too low P . The same applies for the combination $i = 34^\circ$, $\theta_c = 33^\circ$, in which case our line of sight is just outside the cone, but P is only 15%. P agrees better with observations if i and θ_c are closer to the upper and lower limits, respectively, but in this case their difference $i - \theta_c = 29^\circ$ is too large. If we limit the half opening cone angle to be $\lesssim 40^\circ$ constrained by the *HST* image of Hines et al. and Armus et al. (1999), the difference $i - \theta_c$ is minimized to $\lesssim 10^\circ$ for $i \sim 50^\circ$ and $\theta_c \sim 40^\circ$. Therefore, this appears to be the best scattering geometry for IRAS P09104+4109 consistent with observations.

5. Summary and Conclusions

Our high-quality Keck spectropolarimetric and imaging polarimetric data confirm the high polarization and broad Balmer emission lines in the polarized flux spectra of IRAS P09104+4109. In addition, we also detect broad Mg II in both total and polarized flux spectra of the nuclear and extension regions, indicating the presence of a hidden quasar visible only in scattered light. The narrow-line polarizations exhibit a strong positive correlation with line width, critical density and ionization potential of the transition, indicating that the line emission arise from a radially stratified gas. The lack of a clear fan-like morphology in the polarization image suggests that our viewing angle ($i \approx 50^\circ$) is not far outside the ionization cone ($\theta_c \approx 40^\circ$) of IRAS P09104+4109.

The emission-line spectra of IRAS P09104+4109 are consistent with AGN photoionization with contribution from both ionization-bounded and matter-bounded clouds. Under the assumption that photoionization by the central hidden quasar is the main operating mechanism, [Fe VII] should be detected in the extended gas and Mg II should be much stronger than observed. The absence of all Fe lines and weakness of Mg II in the extension can be readily explained if dust is mixed with the ionized gas of the NLR. Furthermore, the fact that both the nuclear and the extended continua are highly polarized with relatively blue polarized flux spectra compared to that of the average quasar also supports the existence of dust, which could efficiently scatter and bluen the light. The other possibility is that the extended gas simply is highly deficient in iron, or is metal poor. This does not seem very likely, since the strengths of the other metal lines appear to be in good agreement with solar abundance. Since grains remain intact, this in turns implies that shocks are probably not important in the extra-nuclear regions. Although the diagnostic diagrams offer somewhat inconclusive assessment of the shocks+precursor models for the extension region, there is no strong evidence for shocks in IRAS P09104+4109 from the line ratios. Ionization by pure shocks can be ruled out by the data. The existence of dust and lack of strong shocks in the extended gas also suggest that it is probably dismembered remnants of a cluster neighbor being disrupted or in the process of merging with the central cD galaxy.

Two predictions follow directly from our interpretation of the current data: The near-IR line [Fe II] $1.257\ \mu\text{m}$ has been observed in the nucleus of IRAS P09104+4109 by Soifer et al. (1996), but should be absent from the extension, confirming the absence of gaseous Fe, and hence the lack of shocks and presence of dust there. Likewise, [Ca II] $\lambda\lambda 7291, 7324$ should be absent in EXT spectrum, since Ca is more than 10 times more sensitive to grain depletion than Fe or Mg (Ferguson et al. 1997b).

We thank P. Ogle and A. Putney for assistance in the observations, and L. Binette for the use of his code Mapping Ic. We are grateful to the referee for several comments, which have improved the clarity of the paper. The W. M. Keck Observatory is operated as a scientific partnership between the California Institute of Technology and the University of California, made possible by the generous financial support of the W. M. Keck Foundation. This research has made use of the NASA/IPAC Extragalactic Database (NED) which is operated by the Jet Propulsion Laboratory, California Institute of Technology, under contract with the National Aeronautics and Space Administration.

REFERENCES

- Allen, M. G., Dopita, M. A., & Tsvetanov, Z. I. 1998, *ApJ*, 493, 571
- Armus, L., Soifer, B. T., & Neugebauer, G. 1999, in “Ultraluminous Galaxies: Monsters or Babies”, *Proc. of the Ringberg Workshop*, 1999, in press, astro-ph/9903332
- Baker, J. C. 1997, *MNRAS*, 286, 23
- Baker, J. C., & Hunstead, R. W. 1995, *ApJ*, 452, L95
- Balsara, D. S., & Krolik, J. H. 1993, *ApJ*, 402, 109
- Barth, A. J., Tran, H. D., Brotherton, M. S., Filippenko, A. V., Ho, L. C., van Breugel, W., Antonucci, R., & Goodrich, R. W. 1999, *AJ*, 118, 1609
- Binette, L., Wilson, A. S., & Storchi-Bergmann, T. 1996, *A&A*, 312, 365
- Binette, L., Wilson, A. S., Raga, A., & Storchi-Bergmann, T. 1997, *A&A*, 327, 909
- Borne, K. D., Bushouse, H., Lucas, R. A., & Colina, L. 2000, *ApJ*, 529, L77
- Brown, J. C., & McLean, I. S. 1977, *A&A*, 57, 141
- Brotherton, M. S., Wills, B. J., Dey, A., van Breugel, W., & Antonucci, R. 1998, *ApJ*, 501, 110
- Burstein, D. & Heiles, C. 1984, *ApJS*, 54, 33
- Cardelli, J. A., Clayton, G. C., & Mathis, J. S. 1989, *ApJ*, 345, 245
- Clark, N. E., Tadhunter, C. N., Morganti, R., Killen, N. E. B., Fosbury, R. A. E., Hook, R. N., Siebert, J., & Shaw, M. A. 1997, *MNRAS*, 286, 558
- Cohen, M. H., Vermeulen, R. C., Ogle, P. M., Tran, H. D., & Goodrich, R. W. 1997, *ApJ*, 484, 193
- Cohen, M. H., Ogle, P. M., Tran, H. D., Goodrich, R. W., & Miller, J. S. 1999, *AJ*, 118, 1963
- Condon, J. J., Huang, Z.-P., Yin, Q. F., & Thuan, T. X. 1991, *ApJ*, 378, 65
- Crawford, C. S., & Vanderriest, C. 1996, *MNRAS*, 283, 1003
- Cutri, R. M., Huchra, J. P., Low, F. J., Brown, R. L., & Vanden Bout, P. A. 1994, *ApJ*, 424, L65
- De Robertis, M. M., & Osterbrock, D. E. 1986, *ApJ*, 301, 727
- De Young, D. S. 1998, *ApJ*, 507, 161
- di Serego Alighieri, S., Cimatti, A., Fosbury, R. A. E., & Hes, R. 1997, *A&A*, 328, 510
- Donahue, M., & Voit, G. M. 1993, *ApJ*, 414, L17

- Dopita, M. A., Koratkar, A. P., Allen, M. G., Tsvetanov, Z. I., Ford, H. C., Bicknell, G. V., & Sutherland, R. S. 1997, *ApJ*, 490, 202
- Dopita, M. A., & Sutherland, R. S. 1995, *ApJ*, 455, 468
- Dopita, M. A., & Sutherland, R. S. 1996, *ApJS*, 102, 161
- Duc, P.-A., Mirabel, I. F., & Maza, J. 1997, *A&AS*, 124, 533
- Evans, A. S., Sanders, D. B., Cutri, R. M., Radford, S. J. E., Surace, J. A., Soloman, P. M., Downes, D., & Kramer, C. 1998, *ApJ*, 506, 205
- Feinstein, C., Macchetto, F. D., Martel, A. R., Sparks, W. B., & McCarthy, P. J. 1999, *ApJ*, 526, 623
- Ferguson, W. J., Korista, K. T., Baldwin, J. A. & Ferland, G. J. 1997, *ApJ*, 487, 122
- Ferguson, W. J., Korista, K. T., & Ferland, G. J. 1997, *ApJS*, 110, 287
- Ferruit P., Binette L., Sutherland R., & Pécontal E. 1997, *A&A*, 322, 73
- Francis, P. J., Hewett, P. C., Foltz, C. B., Chaffee, F. H., Weymann, R. J., & Morris, S. L. 1991, *ApJ*, 373, 465
- Genzel, R., Lutz, D., Sturm, E., Egami, E., Kunze, D., Moorwood, A. F. A., Rigopoulou, D., Spoon, H. W. W., Sternberg, A., Tacconi-Garman, L. E., Tacconi, L., & Thatte, N. 1998, *ApJ*, 498, 579
- Goodrich, R. W., Miller, J. S., Martel, A., Cohen, M., Tran, H. D., Ogle, P. M., & Vermeulen, R. C. 1996, *ApJ*, 456, L9
- Hall, P. B., Ellingson, E., Green R. F. 1997, *AJ*, 113, 1179
- Heckman, T. M., Gonzalez-Delgado, R., Leitherer, C., Meurer, G. R., Krolik, J., Wilson, A. S., Koratkar, A., & Kinney, A. 1997, *ApJ*, 482, 114
- Hes, R., Barthel, P. H., & Fosbury, R. A. E. 1993, *Nature*, 326, 362
- Hines, D. C., & Wills, B. J. 1993, *ApJ*, 415, 82
- Hines, D. C., Schmidt, G. D., Smith, P. S., Cutri, R. M., Low, F. J. 1995, *ApJ*, 450, L1
- Hines, D. C., Schmidt, G. D., Wills, B. J., Smith, P. S., & Sowinski, L. G. 1999, *ApJ*, 512, 145
- Hutchings, J. B., & Neff, S. G. 1988, *AJ*, 96, 1575
- Kingdon, J., Ferland, G. J., & Feibelman, W. A. 1995, *ApJ*, 439, 793

- Kleinmann, S. G., Hamilton, D., Keel, W. C., Wynn-Williams, C. G., Eales, S. A., Becklin, E. E., & Kuntz, K. D. 1988, *ApJ*, 328, 161
- Low, F. J., Huchra, J. P., Kleinmann, S. G., & Cutri, R. M. 1988, *ApJ*, 287, 95
- Maciel, W. J. 1999, *A&A*, 351, L49
- Miller, J. S., & Goodrich, R. W. 1990, *ApJ*, 355, 456
- Miller, J. S., Goodrich, R. W., & Mathews, W. G. 1991, *ApJ*, 378, 47
- Moorwood, A. F. M., Lutz, D., Oliva, E., Marconi, A., Netzer, H., Genzel, R., Sturm, E., & de Graauw, T. 1996, *A&A*, 315, L109
- Murayama, T., Taniguchi, Y., & Iwasawa, K. 1998, *AJ*, 115, 460
- Ogle, P. M., Cohen, M. H., Miller, J. S., Tran, H. D., Fosbury, R. A. E., & Goodrich, R. W. 1997, *ApJ*, 482, L37
- Oke, J. B., Cohen, J. G., Carr, M., Cromer, J., Dingizian, A., Harris, F. H., Labreque, S., Lucinio, R., Schaal, W., Epps, H., & Miller, J. 1995, *PASP*, 107, 375
- Oliva, E., Salvati, M., Moorwood, A. F. M., & Marconi, A. 1994, *A&A*, 288, 457
- Osterbrock, D. E. 1989, *Astrophysics of Gaseous Nebulae and Active Galactic Nuclei*, (Mill Valley: University Science Books)
- Rowan-Robinson, M., Broadhurst, T., Lawrence, A., McMahon, R. G., Lonsdale, C. J., Oliver, S. J., Taylor, A. N., Hacking, P. B., Conrow, T., Saunders, W., Ellis, R. S., Efstathiou, G. P., & Condon, J. J. 1991, *Nature*, 351, 719
- Sanders, D. B., Soifer, B. T., Elias, J. H., Madore, B. F., Mathews, K., Neugebauer, G., Scoville, Z. 1988, *ApJ*, 325, 74
- Sanders, D. B., & Mirabel, I. F. 1996, *ARA&A*, 34, 749
- Scoville, N. Z. et al. 2000, *AJ*, 119, 991
- Soifer, B. T., Neugebauer, G., Armus, L., & Shupe, D. L. 1996, *AJ*, 111, 649
- Storchi-Bergmann, T., Cid Fernandes, R., & Schmitt, H. R. 1998, *ApJ*, 501, 94
- Surace, J. A., Sanders, D. B., Vacca, W. D., Veilleux, S., & Mazzarella, J. M. 1998, *ApJ*, 492, 116
- Tran, H. D. 1995, *ApJ*, 440, 565
- Tran, H. D., Cohen, M. H., & Goodrich, R. W. 1995, *AJ*, 110, 2597

- Tran, H. D., Filippenko, A. V., Schmidt, G. D., Bjorkman, K. S., Jannuzi, B. T., & Smith, P. S. 1997, *PASP*, 109, 489
- Tran, H. D., Cohen, M. H., Ogle, P. M., Goodrich, R. W., & di Serego Alighieri, S. 1998, *ApJ*, 500, 660
- Tran, H. D., Brotherton, M. S., Stanford, S. A., van Breugel, W., Dey, A., Stern, D., & Antonucci, R. 1999, *ApJ*, 516, 85
- Veilleux, S., Kim, D.-C., & Sanders, D. B. 1999, *ApJ*, 522, 113
- Villar-Martin, M., Binette, L., & Fosbury, R. A. E. 1996, *A&A*, 312, 751
- Villar-Martin, M., & Binette, L. 1997, *A&A*, 317, 350
- Villar-Martin, M., Tadhunter, C., Morganti, R., Axon, D., & Koekemoer, A. 1999, *MNRAS*, 307, 24
- Wills, B. J., Wills, D., Evans, N. J., Natta, A., Thompson, K. L., Breger, M., & Sitko, M. L. 1992, *ApJ*, 400, 96
- Wilson, A. S., Binette, L., & Storchi-Bergmann, T. 1997, *ApJ*, 482, 131L

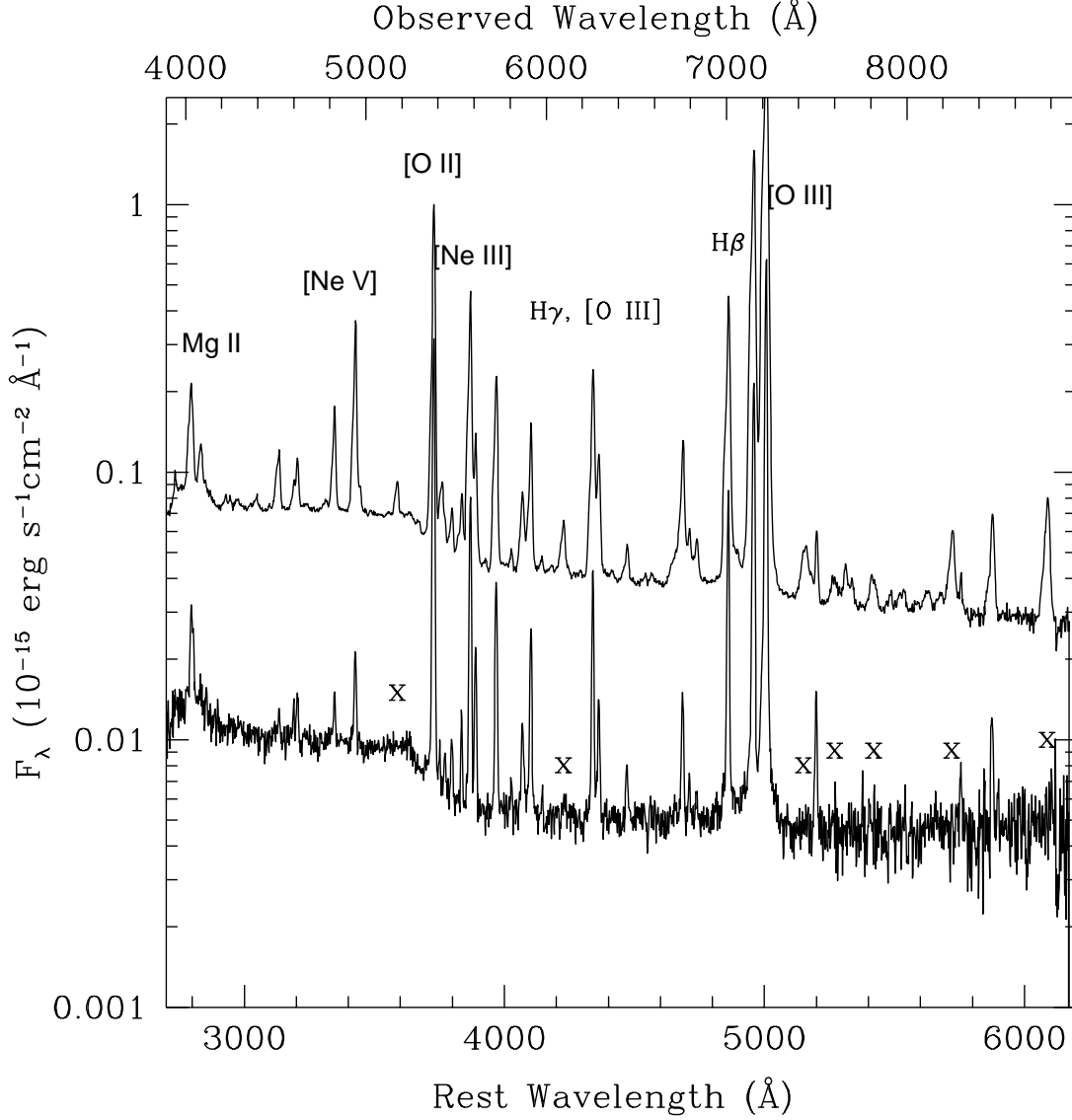


Fig. 1.— Comparison of the total flux spectra of the nucleus (*top*) and off-nuclear NE extension region (*bottom*). “X” denotes where Fe line is expected but not seen in the extension spectrum. Note the complete disappearance of Fe lines, in order from left to right: [Fe VII] $\lambda 3588$, [Fe V] $\lambda 4229$, [Fe VI+VII] $\lambda\lambda 4146, 5159$, [Fe III+VII] $\lambda\lambda 5270, 5276$, [Fe VI] $\lambda\lambda 5424, 5427$, [Fe VII] $\lambda 5720$, [Fe VII] $\lambda 6087$.

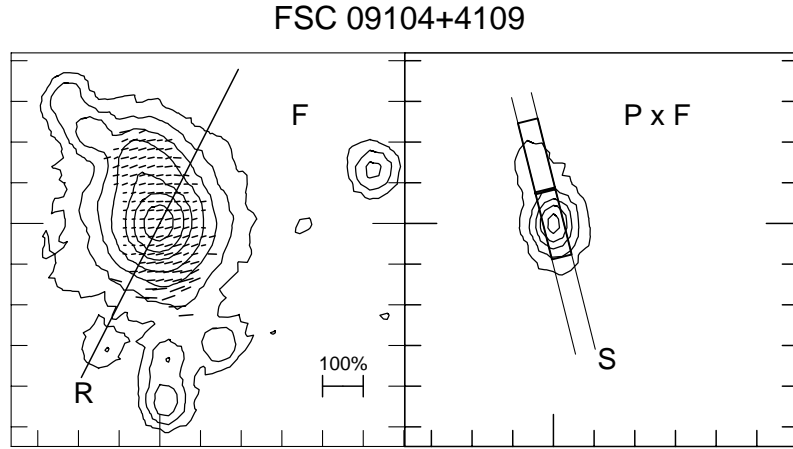


Fig. 2.— Polarization map for IRAS P09104+4109 obtained in B -band with the Keck telescope. The left panel shows the polarization vectors superimposed on the contour plot of the total flux, with north up and east to the left. The scale is $2''$ per tick, and the contours are 0.5, 1, 2, 4, 10, 20, and 50% of the peak. Polarization vectors are shown for those pixels where $P > 2.5\sigma$. The line marked “R” shows the radio axis. A horizontal bar representing 100% polarization is shown at the bottom right. The right panel shows the polarized flux $P \times F$. The contours are 5, 15, 30, 50, and 80% of the peak. The polarized light distribution peaks at the flux peak, suggesting that the observed light is dominated by scattered radiation. The $1''$ wide spectroscopy slit (“S”) is indicated, along with the extraction apertures for the NUC and EXT spectra.

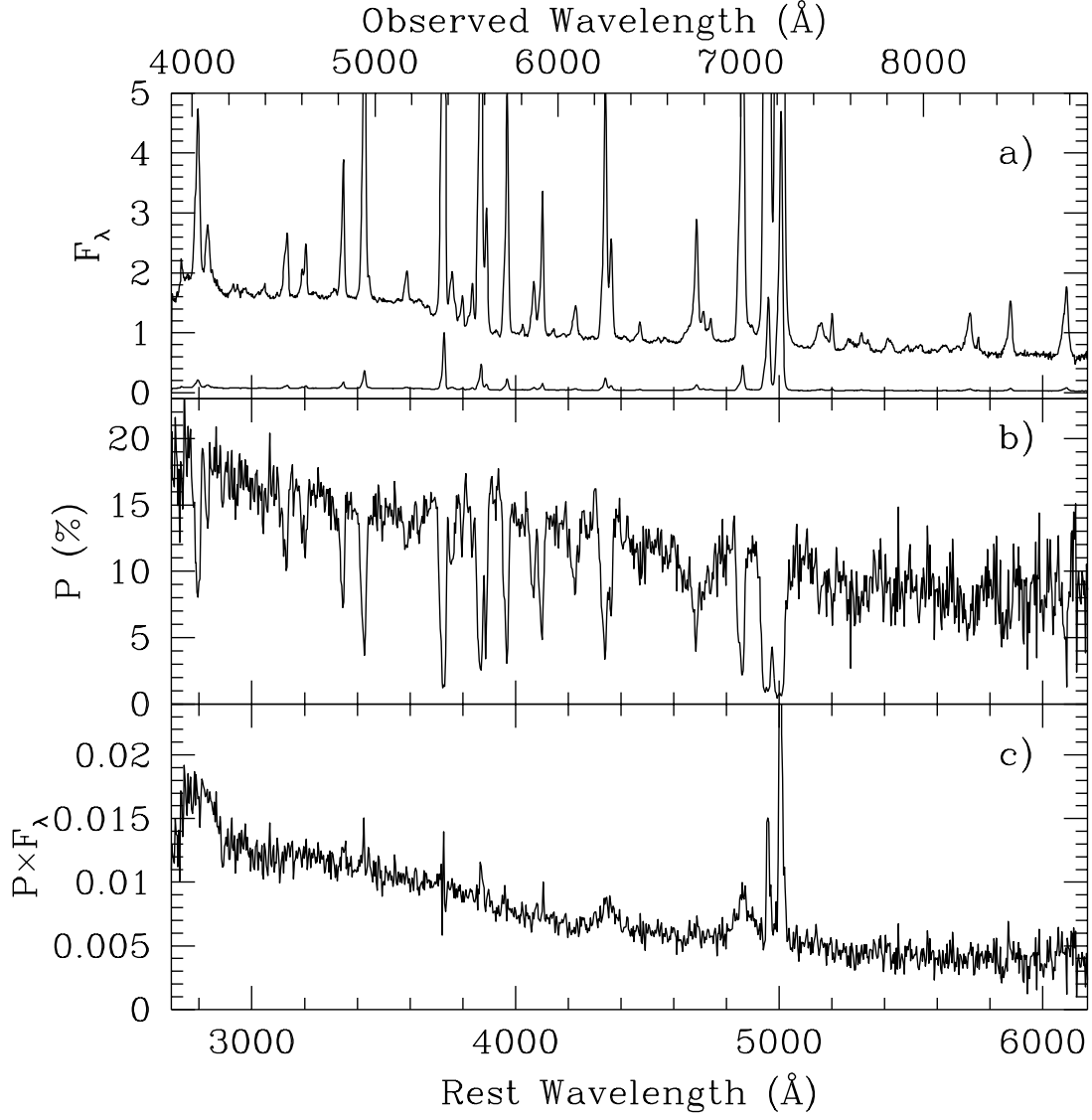


Fig. 3.— Spectropolarimetry of the nucleus of IRAS P09104+4109. (a) Total flux spectrum F_λ , displayed at two scales to show the weaker emission lines, (b) observed degree of polarization P , and (c) polarized flux spectrum $P \times F_\lambda$. The flux scales are in units of 10^{-15} ergs cm $^{-2}$ s $^{-1}$ Å $^{-1}$. Broad H β , H γ , and Mg II, as well as narrow lines of [O III], [Ne V], and [Ne III], are clearly present in the $P \times F_\lambda$ spectrum.

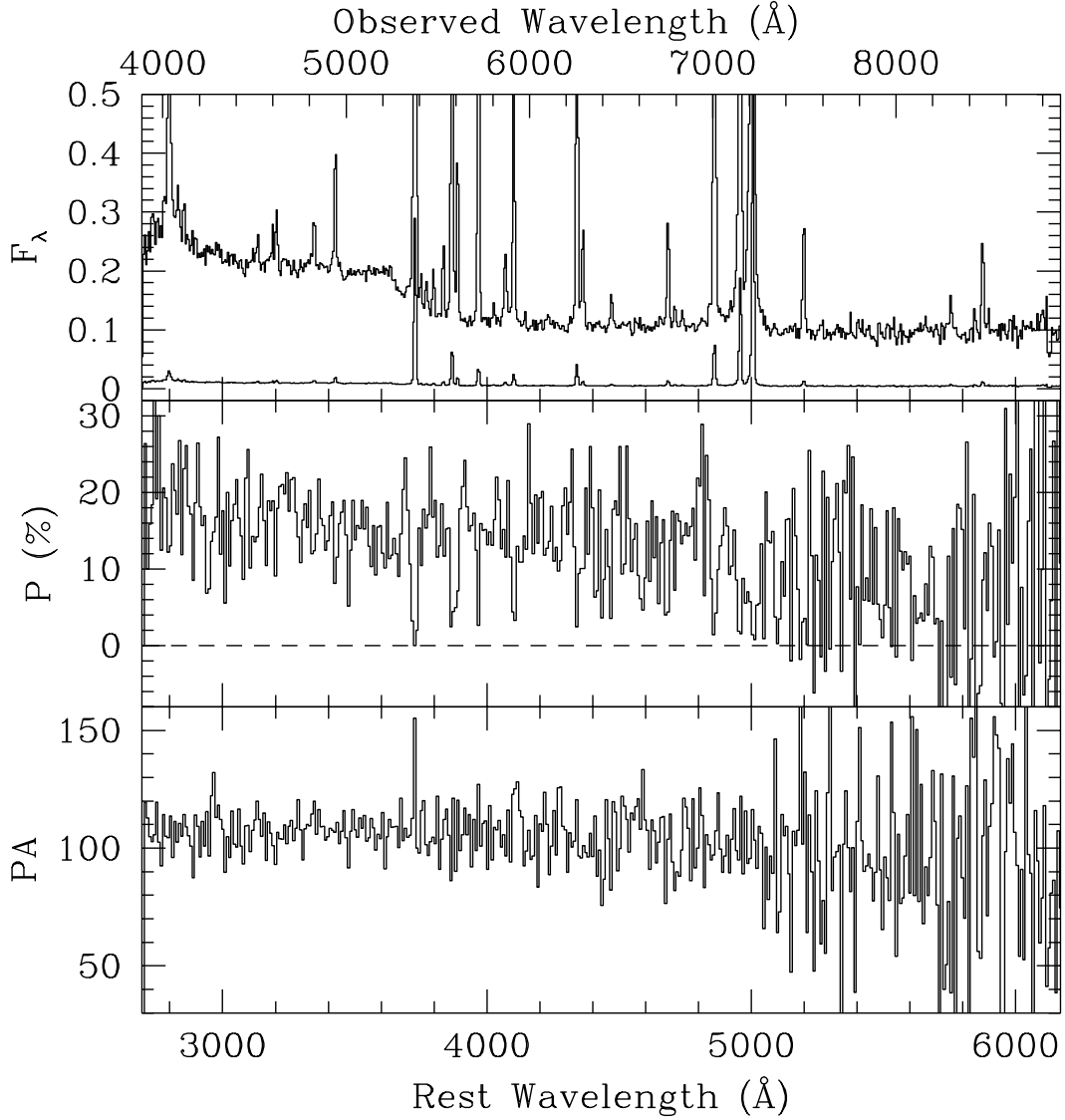


Fig. 4.— Spectropolarimetry of the NE off-nuclear emission line region of IRAS P09104+4109. From top to bottom panels are: the total flux, P , and polarization PA . P and PA have been binned 5 pixels and the flux has been binned 2 pixels. The polarization shows similar high magnitude and wavelength dependence as in the nucleus.

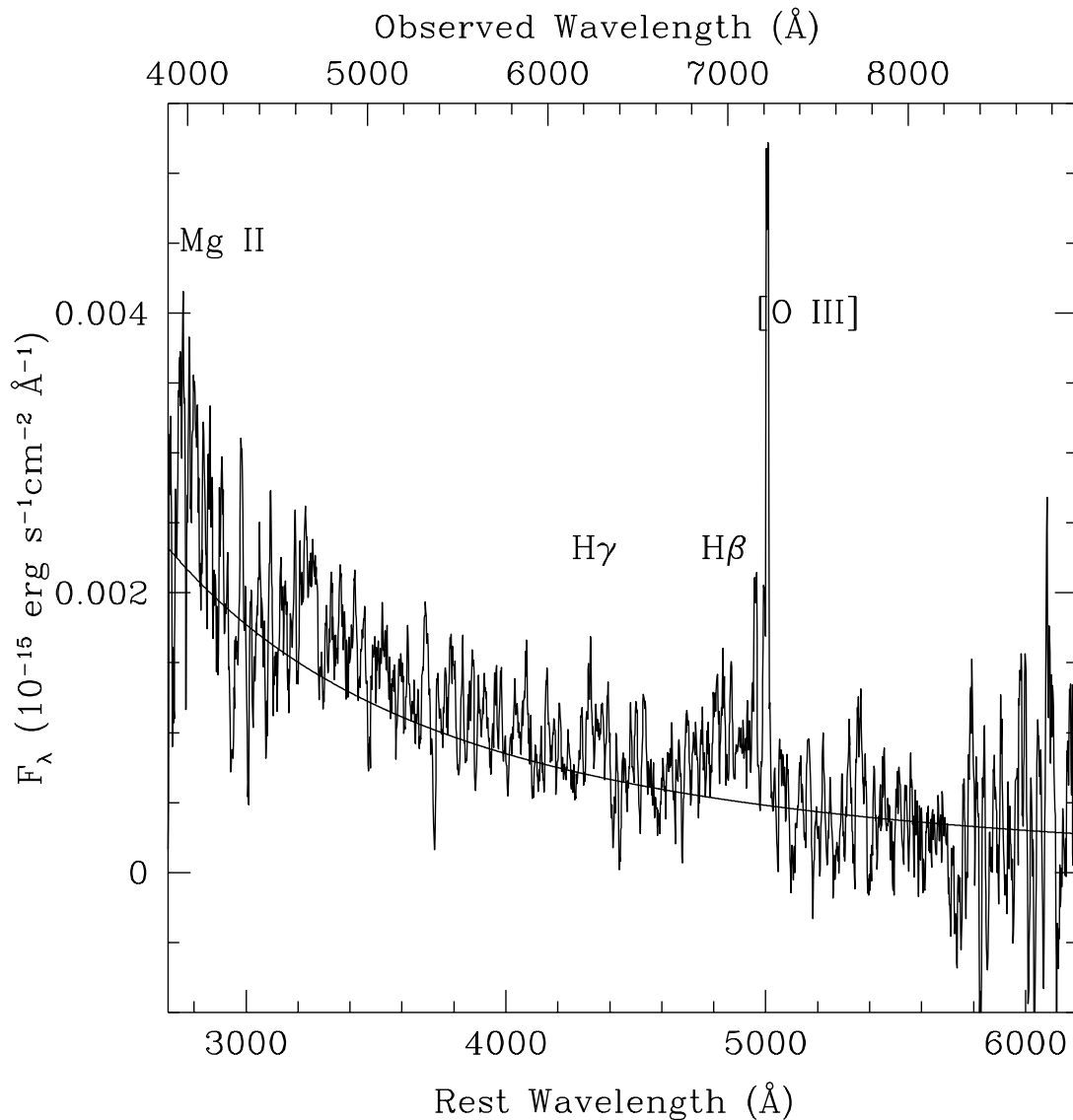


Fig. 5.— The polarized flux spectrum $P \times F_\lambda$ of the extension, smoothed 7 pixels to improve S/N. A broad H β , Mg II and perhaps H γ are visible atop a blue continuum with $\alpha = +0.5$ (solid line, $f_\nu \propto \nu^\alpha$).

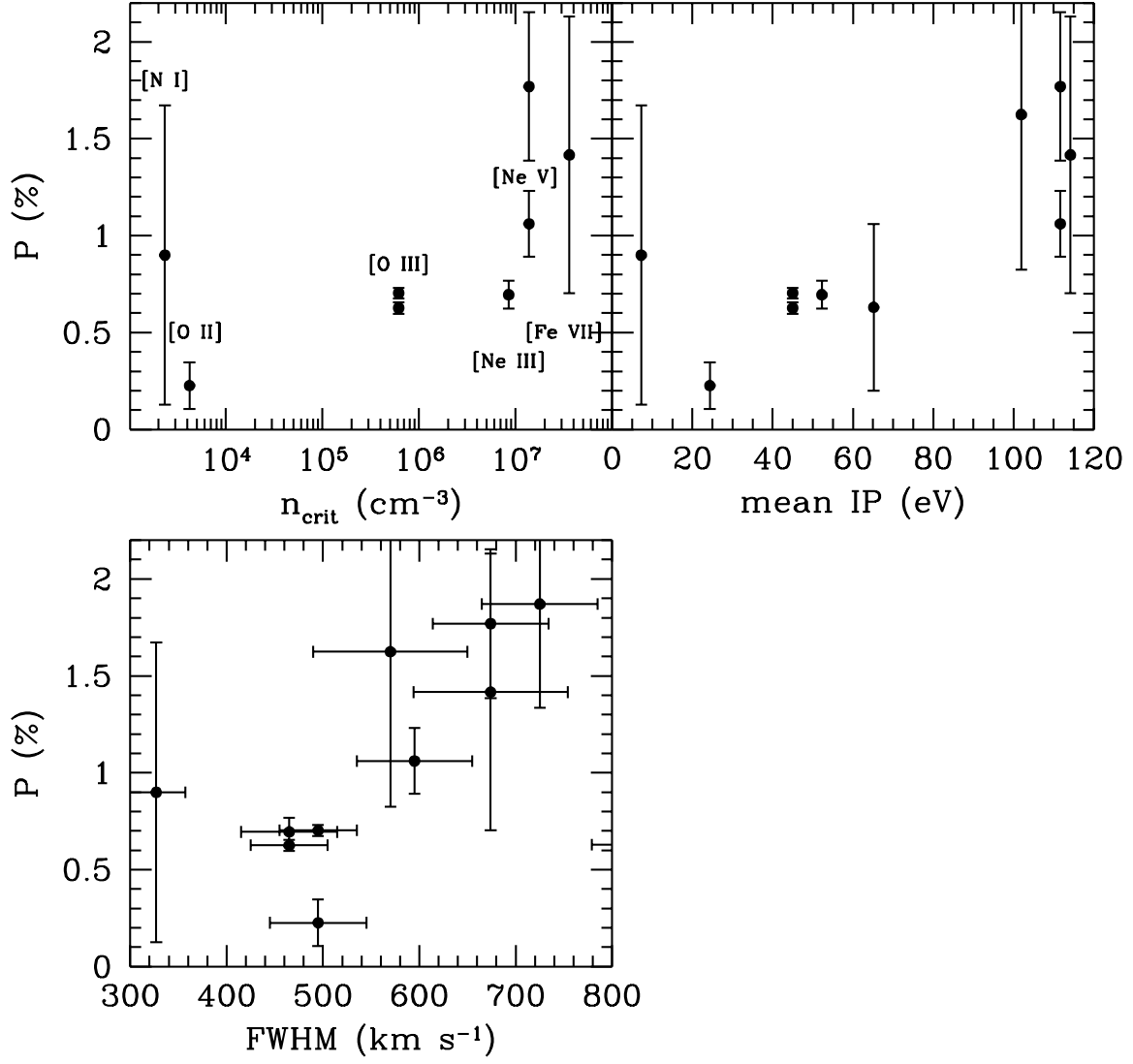


Fig. 6.— Narrow forbidden line polarization as a function of n_{crit} , ionization potential (IP) and line widths. A clear trend of higher polarization with higher n_{crit} , IP, and FWHM is evident.

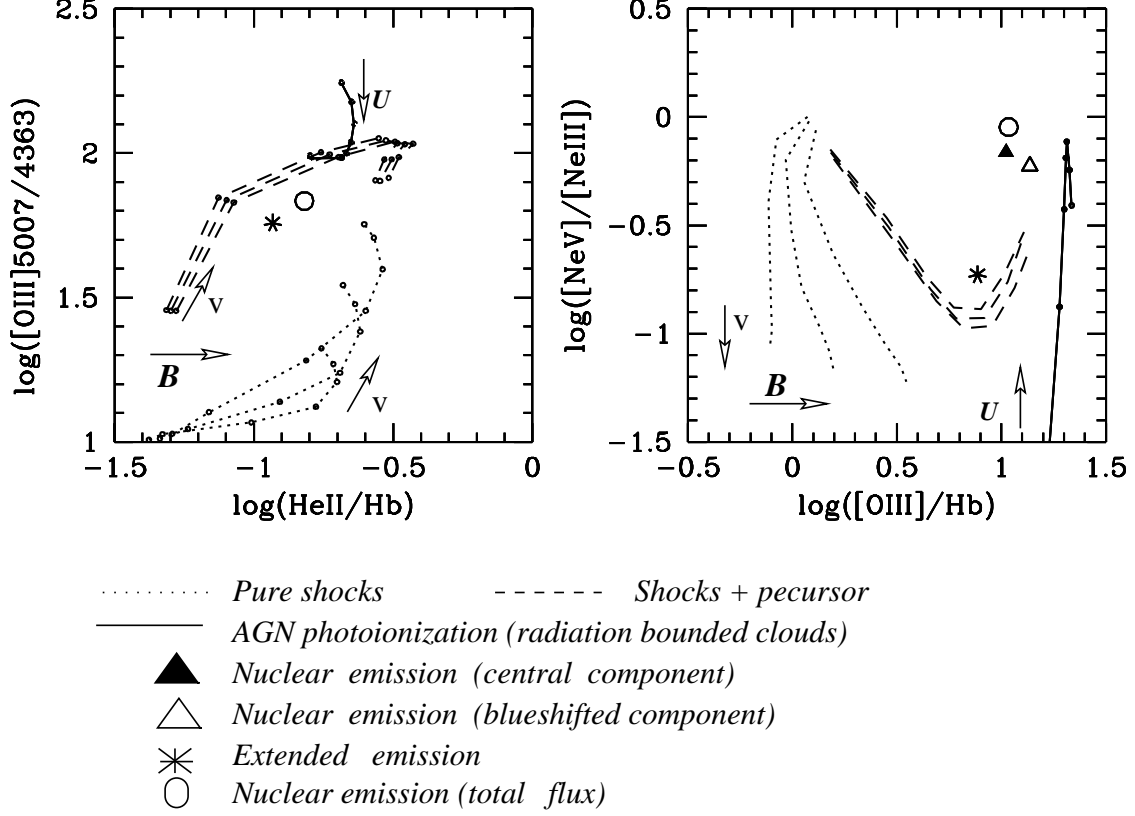


Fig. 7.— Predictions of shock (dotted lines), shock+precursor (dashed lines) and AGN photoionization models with radiation bounded clouds and density $n_e = 10^4 \text{ cm}^{-3}$ (solid lines). U is the ionization parameter that defines the AGN sequence (see text). U varies between 0.001 and 0.46. Each shock (and shock+precursor) sequence is defined by a fixed value of the magnetic parameter B ($B = B/\sqrt{n}$) and a range of shock velocity v (150–500 km s^{-1}). Three shock sequences are shown, corresponding to $B = 1\text{--}4 \mu\text{G cm}^{-3/2}$. These diagrams clearly reject pure shocks (radiative cooling of shocked gas) as the dominant emission line mechanism in the nuclear and extended gas.

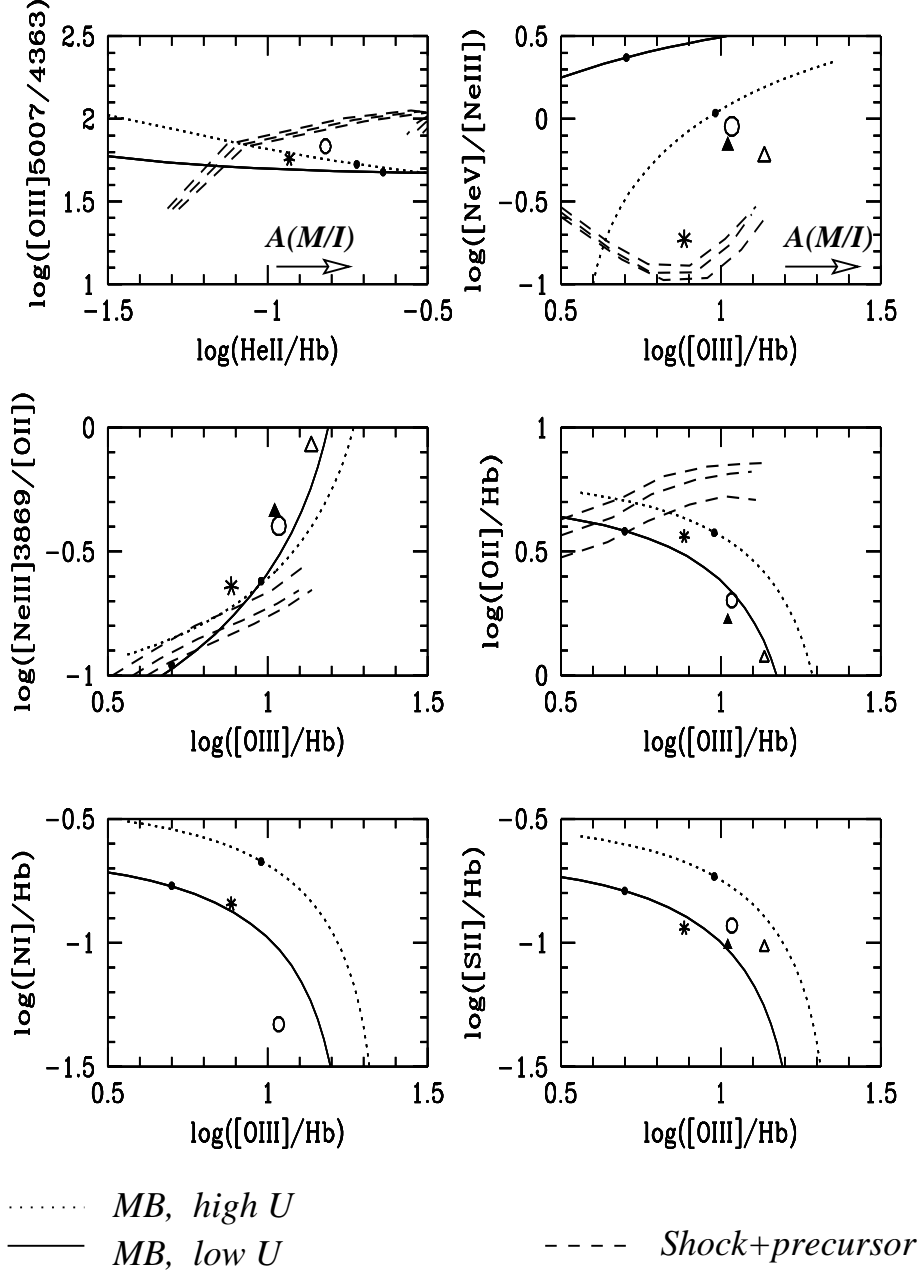


Fig. 8.— Shock+precursor model and AGN photoionization model (with contribution from matter bounded clouds) predictions. The top two diagrams are the same as in Figure 7. The shock+precursor models are plotted only on those diagrams where the calculated line ratios are available. Symbols are as in Figure 7. The filled circles in the MB sequences represent the models with $A_{M/I} = 1$ and the arrow in the upper panels shows increasing $A_{M/I}$. The models with matter and ionization bounded clouds are in good agreement with most line ratios except $[Ne\ V]/[Ne\ III]$, whose predicted values are too high compared with the measurements. These diagrams reject shock+precursor models for the nuclear emission, where, therefore, AGN photoionization dominates. The discrimination between AGN photoionization and shock+precursor models is not possible for the extended gas.

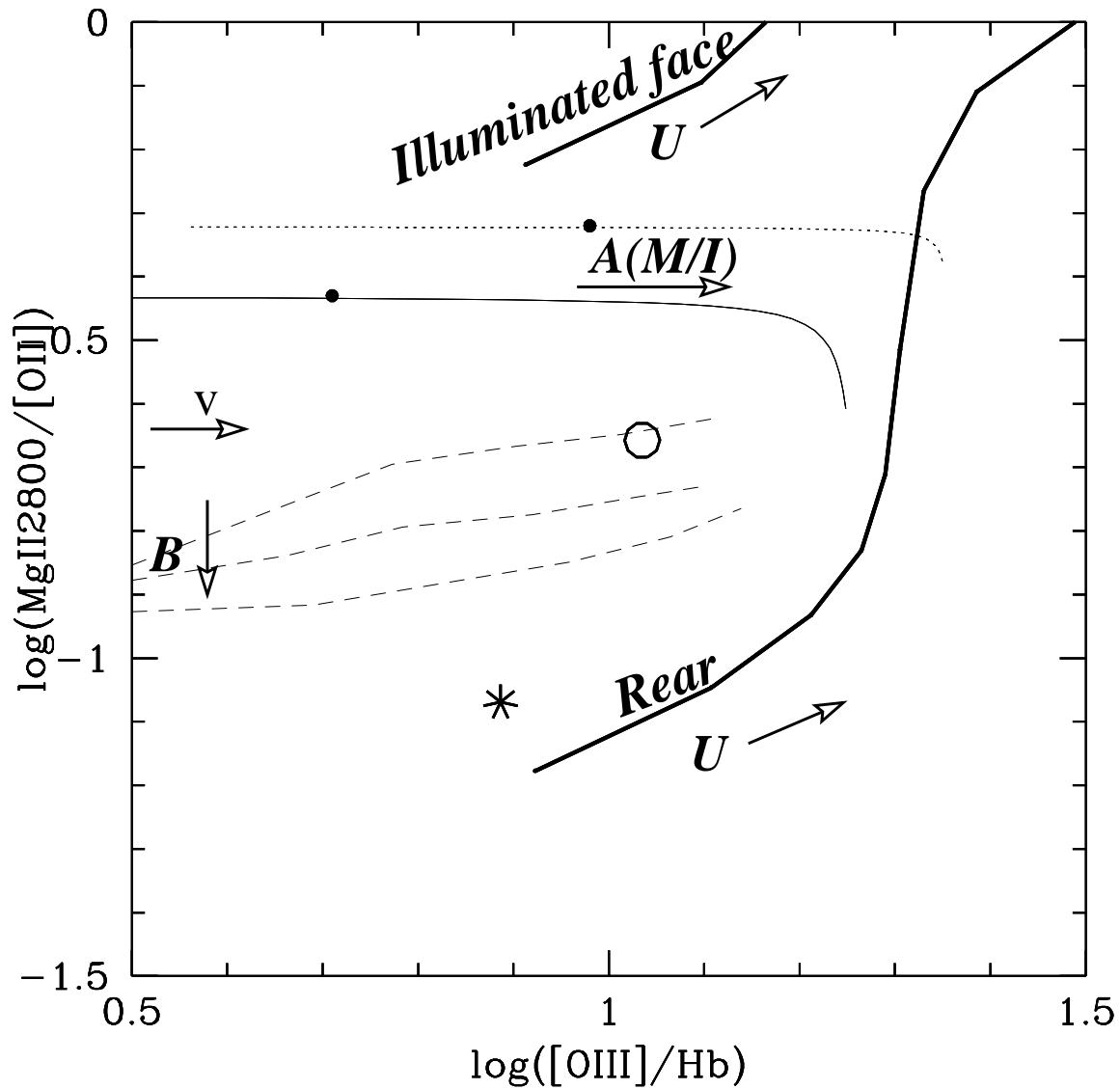


Fig. 9.— $\text{Mg II } \lambda 2800 / [\text{O II}] \lambda 3727$ vs. $[\text{O III}] \lambda 5007 / \text{H}\beta$. The thick solid lines show the photoionization U sequence with radiation bounded clouds as shown in Figure 7, but taking into account perspective effects. The upper sequence corresponds to the clouds seen from the illuminated face and the lower sequence corresponds to the clouds seen from the rear. In this scenario, only the extreme case such that we are inside the ionization cone and see the clouds from the rear could explain the weakness of $\text{Mg II } \lambda 2800$. See text for details. For comparison, shock + precursor and MB photoionization models are also shown. Symbols and lines are as in Figure 8.

Table 1. Emission Line Flux Ratios, Equivalent Widths and FWHMs

Line	IRAS P09104+4109 Nucleus ^a			IRAS P09104+4109 Extension		
	Flux Ratio ^b	EW ^c	FWHM ^d	Flux Ratio ^b	EW ^c	FWHM ^d
He II λ 2733	0.0275	2.7	712			
[Mg V] λ 2783	0.07183	7.0	1449			
Mg II _n λ 2798	0.2584	25.0	1470	0.3110	17.4	840
Mg II _b λ 2798	0.3579	36.	14189	0.71053	55.6	14800
He I λ 2830 + O III λ 2836	0.08345	8.1		0.0324	1.84	
[Ar IV] λ 2854	0.00638	0.52		0.0416	2.74	
[Ar IV] λ 2868	0.00308	0.27				
[Mg V] λ 2928	0.0176	1.8	1481			
He I λ 2946	0.00995	0.95	762			
O III λ 3047	0.0355	3.45				
O III λ 3133	0.1217	11.74		0.0367	2.79	
He I λ 3188	0.0434	4.2	1200	0.0361	2.78	
He II λ 3203	0.05546	5.3	635	0.06463	5.09	
O III λ 3312	0.0200	2.0				
[Ne V] λ 3346	0.2054	20.0	811, 674	0.07033	5.65	
[Ne V] λ 3426	0.5339	53.1	811, 595	0.1561	12.7	
O III λ 3444	0.0406	4.03	1044			
[Fe VII] λ 3588	0.0476	4.76	635, 635			
[O II] λ 3727	1.556	185.0	762, 495	3.646	377.	
H12 (+ H11)	0.1185	15.6		0.0326	3.82	
H11		0.0408	5.1	
H10	0.0429	5.93		0.0588	8.08	
H9	0.0667	9.25		0.0734	10.2	
[Ne III] λ 3869	0.8060	121.7	725, 465	0.8343	123.3	
H8 + He I λ 3889	0.1807	27.9	600	0.1918	29.6	
H ϵ λ 3970 + [Ne III] λ 3967	0.3824	62.3	628, 580	0.4041	59.2	
He I λ 4026	0.0112	1.8		0.0203	2.9	
[S II] λ 4071	0.09695	15.9	712, 750	0.1145	17.0	
H δ λ 4102	0.2163	35.4	835, 465	0.2705	41.1	
He I λ 4144	0.00980	1.6		0.0134	2.05	
[Fe V] λ 4229	0.07158	12.0	918, 859			
H γ λ 4340	0.4127	70.8	731, 480	0.4655	73.9	
[O III] λ 4363	0.1588	27.1	567	0.1343	22.0	
He I λ 4471	0.0359	6.4	906, 433	0.0417	6.40	
He II λ 4686 _n	0.1518	27.6	400	0.1169	17.4	
He II λ 4686 _b	0.1861	34.0	5020			
[Ar IV] λ 4712	0.0150	2.7		0.0245	3.73	
[Ar IV] λ 4740	0.0193	3.5		0.025	3.90	
H β λ 4861	1.000	184.	660, 465	1.000	140.0	
[O III] λ 4959	3.794	1050.	687, 495	2.574	369.5	
[O III] λ 5007	11.18	3541.	700, 465	7.701	1084.	

Table 1—Continued

Line	IRAS P09104+4109 Nucleus ^a			IRAS P09104+4109 Extension		
	Flux Ratio ^b	EW ^c	FWHM ^d	Flux Ratio ^b	EW ^c	FWHM ^d
[Fe VI] λ 5146	0.0318	6.36	567			
[Fe VII] λ 5159	0.0376	8.0	560			
[Fe VI] λ 5176	0.0289	5.82				
[N I] λ 5200	0.05011	11.0		0.1436	24.9	
[Fe III + Fe VII + Fe II] ^e	0.0378	8.3				
[Ca V] λ 5309	0.0361	8.0				
[Fe II + Fe VI] ^f	0.0225	5.0				
[Fe III + Fe VI] ^g	0.0436	9.96				
[Fe VI] λ 5485	0.0142	3.26				
[Cl III] λ 5518	0.0117	2.46				
[Cl III] λ 5538	0.0149	3.14				
[Ca VII] + [Fe VI] ^h	0.0209	4.72				
[Fe VI] λ 5677	0.0153	3.44				
[Fe VII] λ 5720	0.1142	26.5				
[N II] λ 5755	0.0137	3.73		0.0359	5.91	
He I λ 5876	0.1174	29.5	680, 510	0.1028	17.7	
[Fe VII] λ 6087	0.1805	46.3	774, 674			

^aFlux ratios and EWs are measured from starlight-subtracted spectrum.

^bObserved line flux ratios relative to narrow H β . Values for the nucleus are the sum of both the central and blueshifted components corrected for $E(B - V) = 0.24$.

^cRest-frame equivalent widths in Å.

^dFWHMs (km s⁻¹) have been corrected for instrumental resolution of 550 km s⁻¹. The two values for the nucleus denote the central and blueshifted component, respectively.

^eProbable identification: [Fe III] λ 5270 + [Fe VII] λ 5276 + [Fe II] λ 5262.

^fProbable identification: [Fe II] λ 5334 + [Fe VI] λ 5335.

^gProbable identification: [Fe III] λ 5412 + [Fe VI] λ 5424, 5427.

^hProbable identification: [Ca VII] λ 5615 + [Fe VI] λ 5631.

Table 2. Forbidden Line Polarization

Line	P (%)	PA ($^{\circ}$)	Lower IP (eV)	Upper IP (eV)	n_{crit} (cm^{-3})
[Ne V] $\lambda 3346$	1.77 ± 0.38	104.0 ± 6.2	97.1	126.2	1.38×10^7
[Ne V] $\lambda 3426$	1.06 ± 0.17	102.4 ± 4.6	97.1	126.2	1.38×10^7
[O II] $\lambda 3727$	0.23 ± 0.12	124.8 ± 15.2	13.6	35.1	4.20×10^3
[Ne III] $\lambda 3869$	0.70 ± 0.07	93.8 ± 3.0	41.0	63.5	8.48×10^6
[Fe V] $\lambda 4229$	0.63 ± 0.43	56.9 ± 17.7	54.8	75.5	...
[O III] $\lambda 4959$	0.70 ± 0.03	87.7 ± 1.1	35.1	54.9	6.16×10^5
[O III] $\lambda 5007$	0.63 ± 0.03	85.8 ± 1.3	35.1	54.9	6.16×10^5
[N I] $\lambda 5200$	0.90 ± 0.77	118.0 ± 24.6	0.0	14.5	2.34×10^3
[Fe VII] $\lambda 6087$	1.42 ± 0.71	68.4 ± 14.4	100.0	128.3	3.6×10^7